CHEMISTRY OF MATERIALS

pubs.acs.org/cm

Article

Thin-Film Paradigm to Probe Interfacial Diffusion during Solid-State Metathesis Reactions

Rebecca D. McAuliffe,* Guanglong Huang, David Montiel, Apurva Mehta, Ryan C. Davis, Victoria Petrova, Katie L. Browning, James R. Neilson, Ping Liu, Katsuyo Thornton, and Gabriel M. Veith*

Cite This: *Chem. Mater.* 2022, 34, 6279–6287

Read Online

ACCESS | Metrics & More | Article Recommendations | Supporting Information

ABSTRACT: We highlight a paradigm for studying complex reaction mechanisms that guide the synthesis of materials. Thin films of $FeCl_2$ and Na_2S_2 were deposited to study the metathesis reaction to form FeS_2 and NaCl. In situ X-ray reflectivity was used to monitor the interface between materials, which revealed a slow, impeded reaction at high temperatures as compared to previous studies using powder samples. AC impedance and X-ray photoelectron spectroscopy provided insight into distribution of elements and conductivity of the phases present during the reaction, and phase-field modeling was used to elucidate the diffusion of ions throughout the thin-film bilayers. The use of thin-film bilayers provides a simplified system to study solid-state metathesis reactions and highlights the complexity of diffusion at solid-state interfaces.

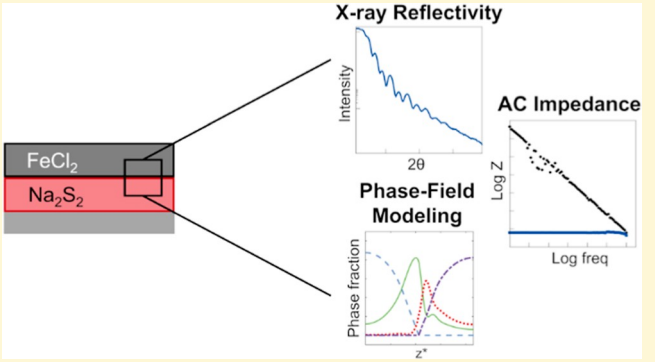

INTRODUCTION

High-throughput ab initio calculations and machine learning have demonstrated the ability to predict new functional inorganic compounds and determine their efficacy for applications such as topological insulators,[1,2] thermoelectric devices,[3,4] and superconductors.[5] The challenge is determining synthesis techniques to realize these compounds.[6−8] An understanding of how to precisely control the movement of atoms is needed to direct the synthesis of materials and achieve the necessary spatial orientation of atoms. While thermodynamics can now be used to estimate reaction pathways and selectivity, the complex nature of time-dependent mass transport remains unwieldy.[9−13] In the case of solid-state reactions of ionic compounds, the processes that mediate interdiffusion of ions must be understood to realize predictive synthesis.

While high-temperature reactions are known to yield thermodynamically stable products, reactions that occur at lower temperatures enable kinetic control of products and provide access to metastable compounds. Metathesis, or double-exchange, reactions follow the generalized reaction formula (AB + CD → AD + CB) and occur at lower temperatures as they are driven by the formation of a thermodynamically stable byproduct (e.g., NaCl or other stable salts).[6] Metathesis reactions have been used to synthesize a range of compounds including transition-metal chalcogenides[14−16] and complex oxides.[17−19] These reactions also provide selectivity as the resulting product can be changed by altering the composition or structure of the precursor materials.[18,19]

Metathesis reactions are often performed by grinding together precursor powders and heating the mixture in a furnace. In the mixture, there are many different crystallite orientations present, creating a complex framework for the diffusion of ions. The reaction pathways are often inferred from diffraction measurements which provide the phases present and the changes in the crystal structures, but as diffraction is a bulk technique, it does not directly monitor the diffusion of ions across the interfaces or the phase boundary information.[16,18−20] To reduce system complexity present in powder-based solid-state reactions, thin-film bilayers are used to study interdiffusion of ions during metathesis reactions and evaluate the importance of various diffusion processes.[21−23]

X-ray reflectivity (XRR) provides direct evidence for the interdiffusion of ions across buried interfaces within thin-film bilayers. The thickness, density, and surface and interfacial roughness of thin film layers can all be independently modeled

Received: January 29, 2022
Revised: June 19, 2022
Published: July 1, 2022

as a function of reaction time and temperature. XRR measurements have been used to observe interdiffusion and formation kinetics of thin-film bilayers as well as to probe reaction mechanisms in the formation of metastable materials using modulated elemental reactants.[24−41] Most studies focus on the synthesis of a single-composition thin film, where precursor films react to form one product, such as the reaction of two metal oxides to form a spinel material, which can be coupled to form more complex layered thin-film structures.[36−41]

In this work, XRR was used to understand the ionic transport that occurs during the solid-state metathesis reaction to form FeS_2 from Na_2S_2 and $FeCl_2$. In situ XRR measurements were performed at several temperatures to monitor the diffusion of ions during the reaction. AC impedance was used to identify the presence of the electrically conductive FeS_2 product, transmission electron microscopy (TEM) was used to confirm product formation, and X-ray photoelectron spectroscopy (XPS) was used to confirm the diffusion of ions across the interface by tracking the relative concentration of elements at the surface. Together, these techniques provide insights into how ions diffuse and exchange during this metathesis reaction, which can be used to inform a phase field model to understand and predict how the reaction progresses throughout the bilayer.

METHODS

Thin films of $FeCl_2$ and Na_2S_2 were deposited using radio frequency magnetron sputtering located within an Ar-filled glovebox as described in previous publications.[42,43] As Na_2S_2 films are more air- and moisture-sensitive than $FeCl_2$, Na_2S_2 was deposited directly onto the Si wafer and then $FeCl_2$ was deposited onto the Na_2S_2 film. Na_2S_2 was deposited at 85 W under 20 cm^3 of Ar at a pressure of 20 mTorr for 100 min. $FeCl_2$ was deposited at 60 W under 20 cm^3 of Ar at a pressure of 20 mTorr for 90 min. The final films were bilayers of $Na_2S_2/FeCl_2$ on untreated 1″ Si wafers, and the layer thicknesses were determined with XRR.

XRR measurements were performed at beamline 7-2 at the Stanford Synchrotron Radiation Lightsource (SSRL) at SLAC National Accelerator Laboratory. The samples were loaded into an Anton-Paar domed heating stage with a polyether ether ketone (PEEK) dome in an Ar-filled glove bag that was purged three times before loading the samples and were measured under flowing He. The samples were measured with a beam energy of 14 keV (λ = 0.8856 Å) and were aligned upon reaching each measurement temperature. XRR data were fit using GenX 2.4.9.[44] Grazing incidence X-ray diffraction (GIXRD) measurements were performed after each XRR measurement. The data are provided in Section S1 of the Supporting Information.

XPS was performed using a PHI 3056 XPS spectrometer operating at 350 W and 15 kV with a Mg Kα (1253.6 eV) source. Samples were prepared in an Ar-filled glovebox and transferred to the XPS chamber under Ar. Survey scans were measured at a 93.9 eV pass energy with 0.5 eV energy steps, and high-resolution scans were obtained at a 23.5 eV pass energy with 0.05 eV energy steps. Spectra were shifted according to the C 1s peak at 284.8 eV to correct for charging. Spectra were fit using MultiPak v8 software.

AC impedance measurements were taken by loading the sample into an Ar-filled glovebox, attaching Kapton-wrapped wires, and placing it in a furnace oven. The wires extended outside the furnace and glovebox to a chi electrochemical workstation 600e. Samples were then heated from room temperature (30 °C) to 250 °C at a rate of 1 °C/min, while AC impedance measurements were taken. AC impedance spectra were taken at a frequency of 2 MHz to 0.1 Hz and at an amplitude of 0.2 V. The spectra were then fitted as an RC circuit to determine the conductivities with EC-Lab software. TEM images were obtained by analyzing a cross-section of the $FeCl_2/Na_2S_2$ bilayer sample deposited on Al_2O_3 that was used for AC impedance experiments. The cross-section was obtained by using an FEI Scios DualBeam FIB/SEM where platinum was first deposited as a surface layer to prevent damage to the sample as a thin section was milled. TEM images were obtained at a 200 keV acceleration voltage on a Thermo Fisher Talos 200X system. Selected area electron diffraction (SAED) was performed and shows that the sample is polycrystalline with regions of NaCl and FeS_2. The phases were assigned based on the lattice parameters. Images, lattice parameters, and electron diffraction patterns are analyzed using the Gatan Micrograph software and fast Fourier transform tools.

Information from the XRR, XPS, and AC impedance measurements was used to develop a phase-field model to simulate the evolution of ionic concentration (in terms of mole fractions) in solid-state metathesis reactions. For this model, we made the following assumptions: (1) the molar volume of a compound is proportional to the number of constituent ions, (2) the reaction involves neither a reduction−oxidation activity nor intermediate compounds, and (3) sulfur dimers S_2^{2-} diffuse as a unit during the reaction. Thus, the four ionic species being considered in this reaction are Na^+, Fe^{2+}, Cl^-, and S_2^{2-}. The spatially and temporally varying mole fraction of ion i (i = Na^+, Fe^{2+}, Cl^-, and S_2^{2-}) is denoted by $X_i(\boldsymbol{r},t)$. We construct a total free energy functional, $\mathcal{F}$, which depends on the mole fractions of each ion

$$\mathcal{F}(\boldsymbol{X}) = \int_V (f_{\text{bulk}} + f_{\text{gradient}} + f_{\text{constraint}})\, dV \tag{1}$$

where $\boldsymbol{X} = [X_{Na^+}, X_{Fe^{2+}}, X_{Cl^-}, X_{S_2^{2-}}]$, f_{bulk} is a bulk energy density term, f_{gradient} sets a finite width for interfaces, and $f_{\text{constraint}}$ imposes constraints on the sum of mole fractions and of electroneutrality. The expressions of these energy terms can be found in Section S5 in the Supporting Information. The evolution of mole fraction of ion i is obtained via the reduction of the free energy, using a mass conservation equation[45]

$$\frac{\partial X_i(\boldsymbol{r}, t)}{\partial t} = \nabla\cdot\left[M_i \nabla\left(\frac{\delta \mathcal{F}}{\delta X_i}\right)\right] \tag{2}$$

where M_i is the mobility of ion i. More details of this model are discussed in Sections S5−S7 in the Supporting Information, and additional details such as the derivation of the model will be provided in a separate publication.

RESULTS AND DISCUSSION

In situ XRR measurements were performed on thin-film bilayers of Na_2S_2 and $FeCl_2$ to understand the interdiffusion of ions at the interface. To compare the results to prior studies performed on powder samples, step-wise isothermal annealing was performed for 11.5 h at 250 °C and then for 2 h at 275, 300, and 350 °C. Data collected at 300 °C were not included in the discussion due to data collection problems. The metathesis reaction between powders of Na_2S_2 and $FeCl_2$ to form NaCl and FeS_2 proceeds to completion at temperatures above 250 °C according to prior studies.[16,20]

To determine the initial thicknesses of the films within the bilayer, an initial XRR measurement was performed at room temperature (RT) under flowing He gas. The initial XRR pattern could not be modeled using only Na_2S_2 and $FeCl_2$, a third layer of a lower density was needed to provide the best fit to the data. Since the lower-density layer is only needed to model the room-temperature data and is not needed to understand the data collected at elevated temperatures, we suggest that this layer is $FeCl_2{\cdot}2H_2O$. A hydrated surface layer would result due to the hydration of the hygroscopic $FeCl_2$ surface and could have been formed during shipping or sample preparation at the beamline. The removal of this layer at elevated temperatures also suggests that this low-density layer

https://doi.org/10.1021/acs.chemmater.2c00303
Chem. Mater. 2022, 34, 6279−6287

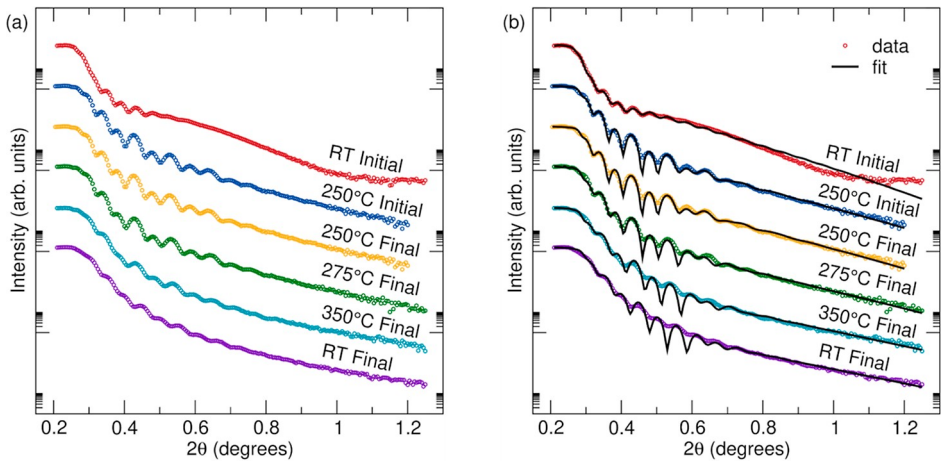

Figure 1. Representative (a) in situ XRR patterns and (b) corresponding simulated fits showing the changes during the reaction.

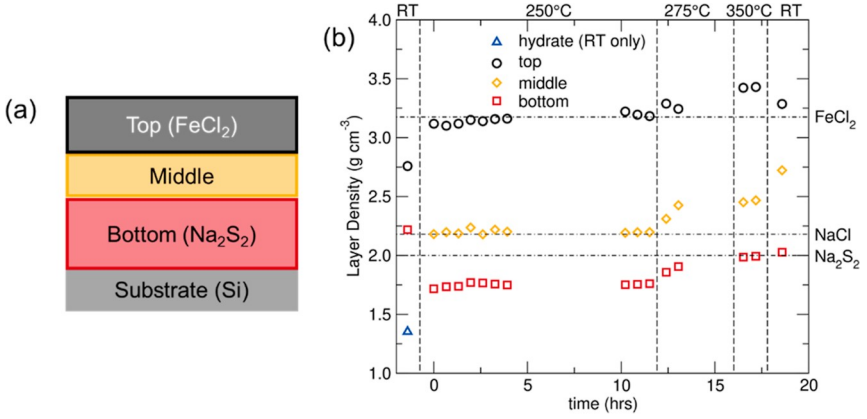

Figure 2. Schematic of layers used to fit XRR data (a) and the values of the layer densities (b) from the simulated fits. Data from the top layer are shown in black circles, the middle layer in yellow diamonds, the bottom layer in red squares, and the low-density hydrate layer in blue triangles. Vertical lines are drawn to denote changes in temperature between the scans. The time is measured from the first scan collected at 250 °C. Horizontal lines are drawn to indicate densities of precursor and product materials. The density of FeS_2 was not included at 5.0 g/cm^3.

is a hydrated surface layer. The three-layer model used to fit the room-temperature data includes (1) a layer of Na_2S_2 (bottom), (2) a layer of $FeCl_2$ (middle), and (3) a layer of $FeCl_2{\cdot}2H_2O$ (top). The total bilayer thickness was fit as ∼860 Å with a Na_2S_2 thickness of ∼560 Å, a $FeCl_2$ thickness of ∼230 Å, and a $FeCl_2{\cdot}2H_2O$ thickness of ∼70 Å. The fit to the room-temperature data is shown in Figure 1b.

Upon heating the sample to 250 °C, there is a distinct change in the XRR pattern that persists throughout the experiment shown in Figure 1. The pattern shows more unique fringes at elevated temperatures and is consistent with the loss of a hydrated surface layer. While there are clear differences from the room temperature and the data collected at 250 °C, no obvious changes were observed during isothermal annealing in the XRR patterns, as shown in Figure 1a. This result indicates that much of the reaction occurred while changing the temperature rather than during the isothermal annealing at 250 °C. The data during the isothermal annealing at 250 °C were fit using a three-layer model with the following layers: (1) a layer of Na_2S_2 (bottom), (2) an interfacial layer (middle), and (3) a layer of $FeCl_2$ (top). A schematic of the model used is shown in Figure 2a, and the simulated fits for selected XRR patterns are shown in Figure 1b. The fit to the first measurement at 250 °C shows an increase in the bilayer thickness from ∼860 to ∼940 Å, which is likely caused in part by the thermal expansion of the film upon heating as well as the formation of defects throughout the layers as ions move to form the interfacial layer. As the time increases at 250 °C, the density of each layer in the three-layer model increases, as shown in Figure 2b. This increase in physical density is consistent with a reaction from Na_2S_2 and $FeCl_2$, which have lower densities of 2.0 and 3.2 g/cm^3, to NaCl and FeS_2, which have higher densities of 2.2 and 5.0 g/cm^3, respectively. To better visualize the change in composition as a function of film thickness, the scattering length density (SLD), which is a function of the scattering power of the material at a given position in the film, was calculated from the fit to the XRR data and is shown in Figure 3. The SLD of each layer in the bilayer increased over the 11.5 h isothermal hold at 250 °C, but the expected final SLDs of 0.63 for NaCl and 1.44 for FeS_2 were never realized. Figure 3 also shows that while the SLDs of the layers increase, the thickness of the layers stays the same through the reaction at 250 °C; this indicates that the interfacial region does not grow or propagate through the bilayer. The values for thickness and roughness of the layers are shown in Figures S3 and S4 in Section S2 of the Supporting Information. Thus, while a reaction appears to be occurring in the bilayers, the progress of the reaction is quite limited and confined to an interfacial region. This is unexpected as

https://doi.org/10.1021/acs.chemmater.2c00303
Chem. Mater. 2022, 34, 6279−6287

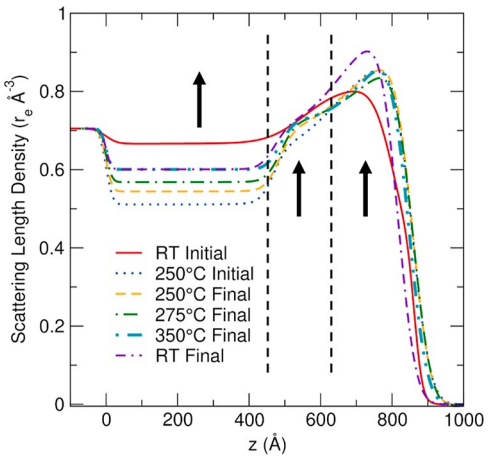

Figure 3. Calculated SLD vs distance from the substrate, *z*. The film increases in thickness upon heating due to thermal expansion at 250 °C and contracts when cooled to room temperature (RT). The density of the RT initial scan is significantly different from that of the 250 °C initial scan, but upon annealing, the density of the film increases, which is consistent with the expected metathesis reaction to form FeS_2.

previous in situ powder XRD data show a reaction occurring quickly upon heating to 250 °C in a bulk powder system.[20]

To further understand the effect of temperature on the interdiffusion of ions during the solid-state metathesis reaction, isothermal annealing of the sample at additional temperatures of 275 and 350 °C was also performed subsequent to the annealing at 250 °C. During the measurements at 275 and 350 °C, the intensity of the fringes decreases, indicating an increase in the physical densities and SLDs of the layers, which is reflected in Figures 2 and 3. The three-layer model used in fitting the data at 250 °C accurately captures the peak locations in the XRR data but does not capture the decrease in intensity, especially at the minima of the Kiessig oscillations. Additional models were tested to capture changes at the interface, shown in Figure S5 in the Supporting Information; however, the three-layer model was the most accurate model for fitting the peak positions and yielded physically reasonable results.

A final XRR measurement was performed at room temperature to observe the changes to the sample without the effect of thermal expansion. The final physical densities of the layers are 3.29, 2.72, and 2.03 g/cm^3, which represent an increase of 5.2, 19.8, and 15.8%, for the top, middle, and bottom layers, respectively, as compared to the initial scan at 250 °C. While there is an overall increase in density, the densities are lower than expected for a completed reaction, for which the expected densities are 2.2 and 5.0 g/cm^3 for NaCl and FeS_2, respectively. The lower observed densities could be due to low crystallinity of the films that would reduce the density, with the reaction not proceeding significantly, the formation of voids, or a lateral distribution of domains with different phases being present within a layer. As an example, if there was a layer with both FeS_2 and NaCl present, the overall density of that layer would be lowered to ~3.1 g/cm^3 assuming a 2:1 formation of NaCl/FeS_2.

While the XRR measurements provide insight into the changes in the scattering densities throughout the bilayer, it is difficult to confirm that the intended products are being formed during the reaction as the reaction does not appear to be complete. Additionally, while the models shown fit the XRR data, the XRR patterns do not correspond to a unique SLD. Therefore, further techniques were used to support the findings from the XRR data. GIXRD measurements were performed after each XRR measurement, as shown in Figure S1 in the Supporting Information. The room-temperature GIXRD pattern shows peaks that remain present throughout the measurement. The strongest peaks, however, are likely from the PEEK dome on the heating stage. At 250 °C, broad, low-intensity peaks and humps are formed, which increase in intensity as the temperature is increased, showing a potential crystallization of a phase. The peak broadness could be due to low crystallinity, a small particle size, or large defect concentrations in the phases. Due to the broad nature of the peaks, it is difficult to determine what phases are present or if peaks are due to multiple phases. Phase identification is difficult due to similar peak positions across several sodium and iron sulfide phases, as shown in Figure S2. Therefore, further complementary techniques were used to characterize the phases formed during the reaction.

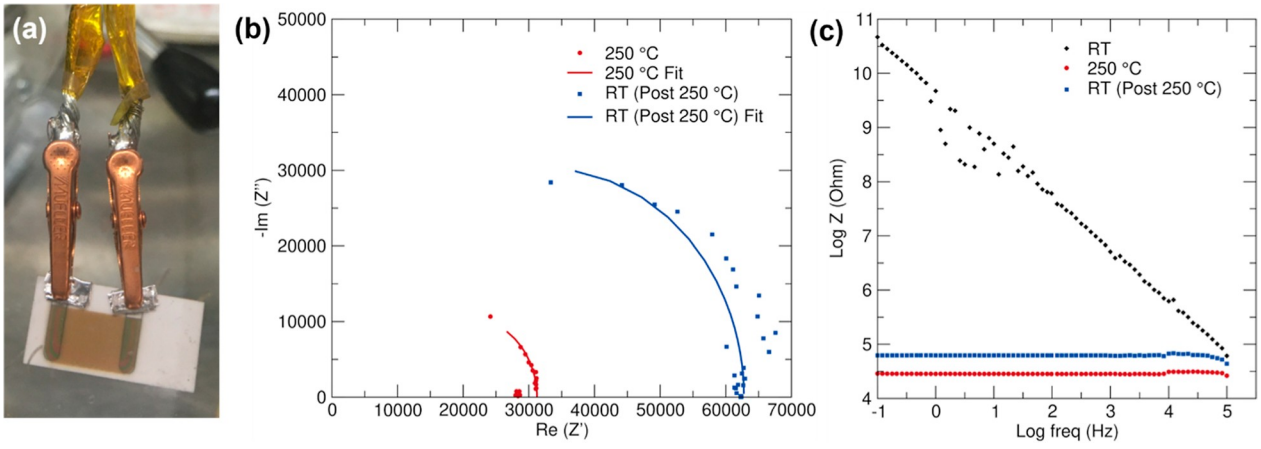

Figure 4. (a) Image of the sample connected to wires for measuring AC impedance during heating. (b) Nyquist plots of impedance measurements at 250 °C and after allowing to cool to room temperature along with simulated fits showing conductivity stability. (c) Bode plot of frequency response at room temperature, 250 °C, and after heating at room temperature, showing an increase in conductivity with heating and subsequent stability.

https://doi.org/10.1021/acs.chemmater.2c00303
Chem. Mater. 2022, 34, 6279−6287

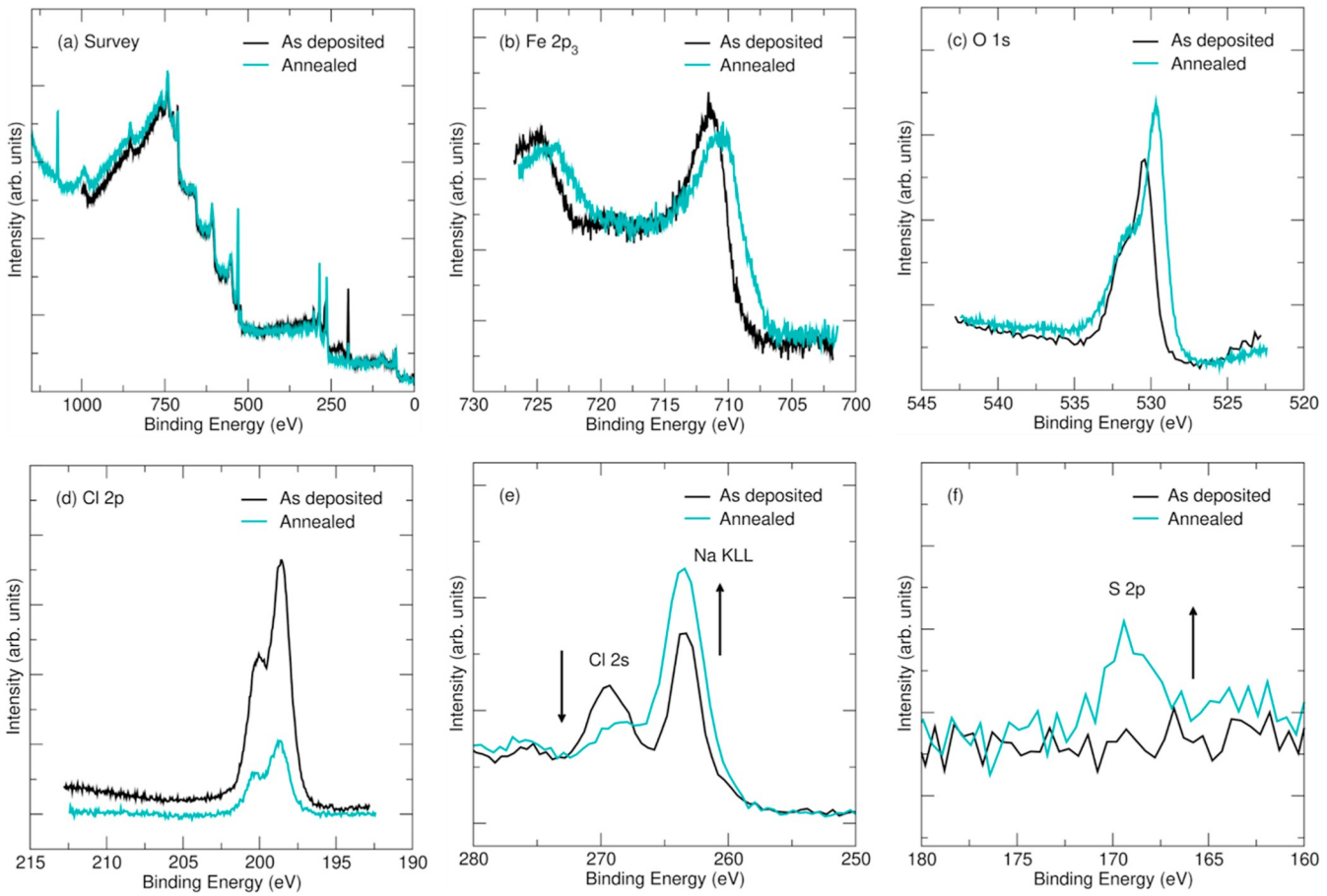

Figure 5. XPS spectra for the as-deposited (black) and annealed samples (light blue). The survey spectra are shown in (a,e,f), and the high-resolution spectra are shown in (b,c,d).

To test for the presence of the products, AC impedance measurements were performed on samples with the same thickness as XRR samples but deposited on top of Ir electrodes, as shown in Figure 4a. AC impedance measurements monitor the changes in conductivity through the sample, and since only FeS_2 is electrically conductive, the formation of FeS_2 can be monitored throughout the bilayer. As the sample is heated, we expect the FeS_2 and NaCl products to form, creating a conducting pathway between the two Ir electrical connectors. The measured conductivity may then be due to either a fully random, connected network or a layer-by-layer mechanism. Figure 4b shows representative impedance data collected at 250 °C and upon cooling to room temperature. The bilayers were initially observed to be insulating and extremely resistive at room temperature. However, at 225 °C, the conductivity of the samples began to increase, and at 250 °C, the conductivity spikes, indicating the formation of an electronically conductive product. The impedance is stable at 250 °C for 3 h at a conductivity of 0.34 S/cm, which is consistent with the XRR measurements that showed that the reaction occurs, but does not progress substantially during an isothermal hold at 250 °C. The conductivity of the sample drops to 0.17 S/cm upon cooling, as can be seen in the Nyquist plot, shown in Figure 4b, indicating that the conductive products are stable upon cooling to room temperature. The Bode plot, Figure 4c, with the log scales of impedance and frequency clearly shows the initial, insulating nature of the sample at room temperature and the rise in conductance after heating. This rise indicates that a conductive reaction product was formed and is not an effect of temperature on the sample. TEM images along with SAED patterns were collected on a cross-section of the sample that was used for impedance measurements and is shown in Figure S6 in the Supporting Information. Care should be taken when evaluating these data due to the beam sensitivity of sulfides and chlorides. The formation of NaCl and FeS_2 is supported based on the lattice parameters from the SAED data. TEM shows the formation of FeS_2 in the pyrite phase as *d*-spacings of 3.10, 2.67, and 2.43 Å correspond to the *d*-spacings for the (1 1 1), (2 0 0), and (2 1 0) planes, respectively.

To give further insight into the changes in chemical composition resulting from the metathesis reaction, XPS measurements were performed on the as-deposited and annealed films. The survey scans for both samples are shown in Figure 5a. The spectra of the as-deposited film contain peaks for Fe, Cl, Na, C, and O, while the spectra of the annealed sample contain an additional peak for S, confirming that S diffused through the bilayer. The first Fe $2p_{3/2}$ peak for the as-deposited sample is centered at 711.4 eV, and the second peak is at 724.8 eV, as shown in Figure 5b. The Fe $2p_{3/2}$ peaks for the annealed samples are shifted to lower energies of 710.6 and 723.5 eV, respectively. These initial peaks are consistent with the presence of $FeCl_2$.[46] The broadening of the peak in the annealed sample to lower binding energies may indicate the presence of FeS_2, which has a binding energy around 707 eV.[47] The O 1s peaks, shown in Figure 5c, are similarly shifted to

https://doi.org/10.1021/acs.chemmater.2c00303
Chem. Mater. 2022, 34, 6279−6287

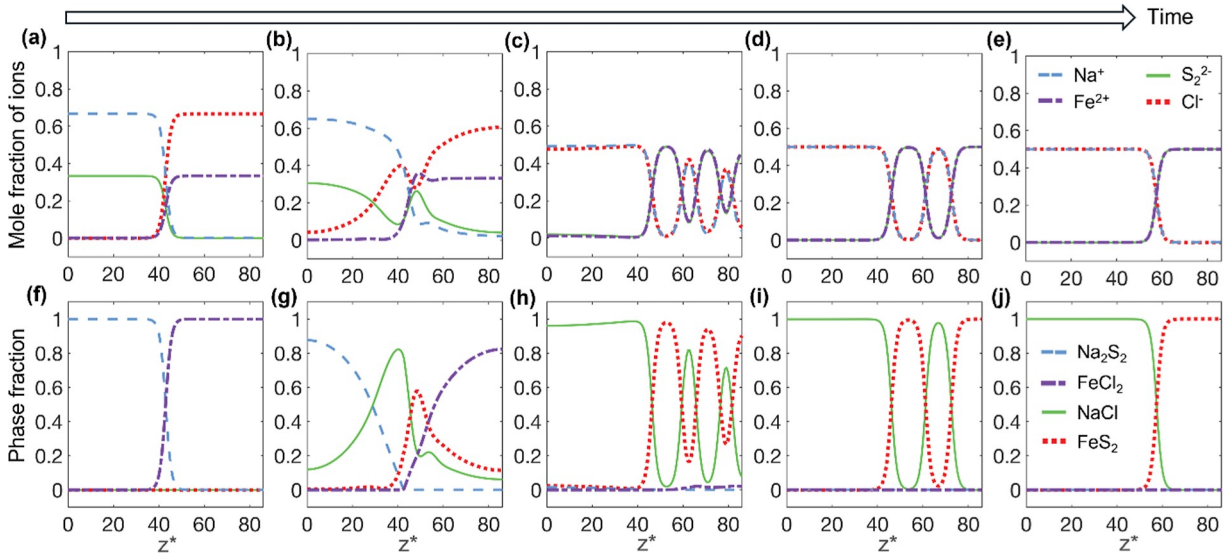

Figure 6. Evolution of (a−e) mole fraction of ions and (f−j) phase fractions. The unit length of the horizontal (z) axis is equivalent to 1 nm.

lower energies with the as-deposited peaks present at 531.4 and 531.7 eV and the annealed peaks at 529.7 and 530.4 eV. The presence of two O 1s peaks indicates that there are multiple oxygen bonding states present at the surface of the film, potentially due to hydration of the hygroscopic surface during sample preparation, consistent with the XRR results. The Cl 2p peak is also observed in both spectra and is shown in Figure 5d; however, the peak is more than 3.5 times smaller in the annealed sample. This indicates there is less Cl present at the surface after annealing and that Cl likely diffuses away from the surface and deeper into the film. While it is possible that Cl is also lost to the surrounding environment, previous studies on powders have shown that Cl is not released as a gas during the reaction; however, evidence of sulfur vapor evolution was observed.[16] The Cl 2p peaks are in similar locations in the as-deposited and annealed films with peaks at 198.6 and 200.1 eV for the as-deposited film and 198.7 and 200.3 eV for the annealed film, which are expected energies for alkali or metal chlorides.[48] The Na 1s peak is present in the annealed sample at a binding energy of 1072.2 eV, which corresponds with the presence of NaCl.[48,49] The survey scans also show that the Na KLL Auger peak at 263.6 eV is present in both the as-deposited and annealed samples. Figure 5e shows how the Na KLL peak is larger and the Cl 2s peak is smaller in the annealed sample, indicating that Na diffuses to the surface and Cl diffuses into the film during annealing. The S 2p peak is only present in the annealed sample at a binding energy of 168.8 eV. This peak is at a higher binding energy than expected for a metal sulfide compound and is more consistent with a sulfate at the surface of the film. This may be due to the reaction between air and sulfur during the transportation of the film after XRR measurements.[48,50] Figure 5f shows that the S peak is only present in the as-annealed sample, indicating that S migrates to the surface during the annealing process.

The XPS data indicate that S and Cl are the mobile species during the metathesis reaction. While Na diffuses through the bilayer, it primarily stays near the substrate. Fe is the least mobile species during the reaction. By estimating the relative mobilities of the ions, phase-field modeling can be performed to simulate the evolution of the phases and compositions within the bilayer. Based on XPS data, we assigned a low mobility to Fe^{2+} and a high mobility to S_2^{2-} and Cl^-. We assigned the highest mobility for Na^+ because the self-diffusion coefficient of Na^+ is higher than that of Cl^- in crystal NaCl, as previously reported.[51−54] All mobilities are assumed to be constant, independent of the phases, which is a simplifying assumption. The interfacial thickness employed in the phase-field model is chosen to be 5 nm, which is estimated based on the average thickness of the regions with the SLD gradient observed in Figure 3. The non-dimensionalization of phase-field variables and their values are summarized in S6 and Table S2 in the Supporting Information, respectively. The evolution of mole fraction of ions and phase fractions is shown in the first and the second row of Figure 6, respectively.

It can be observed from the Figure 6a,b,f,g) that S_2^{2-} and Na^+ ions diffuse to the right of the simulation domain (toward the surface of the thin film), while Cl^- ions diffuse to the left (toward the substrate) during the early stage of the simulation. This is followed by the formation of the NaCl region on the left side of the domain (adjacent to the substrate). Rapid formation of NaCl can be attributed to the large reduction of free energy by its formation, which is a benefit of metathesis reactions. The simulation further predicts phase separations between FeS_2 and NaCl subsequently (see Figure 6c,h) on the right side of the simulation domain, where all four ions are present in various amounts. The Na^+ and Cl^- ions at the right side then gradually diffuse to the left, resulting in disappearance of NaCl phases (see Figure 6d,i,e,j). The simulation reaches an equilibrium when the NaCl and the FeS_2 phases occupy the left and right sides of the simulation domain, respectively.

The progression of the metathesis reaction was initially assumed to proceed through a planar reaction front moving from the interface through the volume of the bilayer. However, XRR, XPS, and phase-field modeling show that based on the mobilities of the ions, the reaction front is complex. In comparing the phase-field modeling with the experimental data, one would expect a higher final SLD corresponding to the formation of the end products, FeS_2 and Na_2S_2. This was not observed during the experiments performed. There are several possible explanations for the difference. First, the planar

https://doi.org/10.1021/acs.chemmater.2c00303
Chem. Mater. 2022, 34, 6279−6287

experiments are still in the early stage of the process simulated, that is, the reaction kinetics is slower than what is predicted based on simulation due to a diffusion barrier. Second, the mobilities are much smaller in the product phases than the reactant phases, leading to the slowdown of the process as the product phases form and block transport. Third, the reaction may not progress in a completely planar reaction front and instead may form in-plane, or lateral, inhomogeneities. Regardless, this work indicates that the reaction process is limited. This is surprising given the fast reaction occurring with powders and indicates that different diffusion processes dominate the metathesis reaction over interfacial transport. This result shows that the interfacial reactions that occur during metathesis reactions are more complicated than originally expected and highlights the need to use complementary techniques, such as XRR, AC impedance, XPS, and phase-field modeling, to begin to capture the diffusion behavior present at interfaces during solid-state reactions. Further imaging of the interface using TEM (compatible with sulfur) and X-ray tomography can provide additional insights to further understand the distribution of phases in the bilayer.

CONCLUSIONS

By utilizing thin-film bilayers, one can gain a simplified glimpse into the diffusion processes during solid-state reactions. While these bilayers simplify the solid-state metathesis reaction in the sense that there are fewer interfaces present and fewer diffusion routes available to the system, the diffusion through the thin-film interface is still complex. In situ XRR showed that the diffusion through the thin film interface is slow and limits the reaction front, while this is not observed in powders with the same chemical system. The geometry of the thin-film system provides a unique model for understanding and probing interfacial diffusion.

Phase-field simulations suggest that the diffusion of ions within the thin-film bilayer results in a rapid formation of NaCl salts adjacent to the substrate, followed by phase separations between FeS_2 and NaCl near the surface of the bilayer. Finally, the FeS_2 phase forms near the surface as Na^+ and Cl^- ions diffuse toward the substrate. While FeS_2 is confirmed to form based on the AC impedance data, no high-density (~1.44 in SLD) layer is observed in the fits to the XRR data. This observation indicates that the reaction performed in the experiment is still at an early stage (as compared to the simulated reaction process), that the reaction slows down due to a lower mobility of ions in the product phases as compared to that in the reactant phases, or that the reaction front is not planar and may form domains with lateral inhomogeneities.

ASSOCIATED CONTENT

Supporting Information

The Supporting Information is available free of charge at https://pubs.acs.org/doi/10.1021/acs.chemmater.2c00303.

GIXRD data, additional data from XRR models, multilayer models of XRR data, TEM of thin-film cross-sections with SAED patterns, free-energy functional of the phase-field model, initialization of mole fractions and determination of phase fractions for the phase-field model, and nondimensionalization of the phase-field equations (PDF)

AUTHOR INFORMATION

Corresponding Authors

Rebecca D. McAuliffe − *Chemical Sciences Division, Oak Ridge National Laboratory, Oak Ridge, Tennessee 37831, United States;* orcid.org/0000-0002-6497-4360; Email: mcaulifferd@ornl.gov

Gabriel M. Veith − *Chemical Sciences Division, Oak Ridge National Laboratory, Oak Ridge, Tennessee 37831, United States;* orcid.org/0000-0002-5186-4461; Email: veithgm@ornl.gov

Authors

Guanglong Huang − *Department of Materials Science and Engineering, University of Michigan, Ann Arbor, Michigan 48109, United States;* orcid.org/0000-0002-2627-0901

David Montiel − *Department of Materials Science and Engineering, University of Michigan, Ann Arbor, Michigan 48109, United States;* orcid.org/0000-0003-3775-2735

Apurva Mehta − *Stanford Synchrotron Radiation Lightsource, SLAC National Accelerator Laboratory, Menlo Park, California 94025, United States;* orcid.org/0000-0003-0870-6932

Ryan C. Davis − *Stanford Synchrotron Radiation Lightsource, SLAC National Accelerator Laboratory, Menlo Park, California 94025, United States*

Victoria Petrova − *Department of Nanoengineering, University of California-San Diego, La Jolla, California 92093, United States*

Katie L. Browning − *Chemical Sciences Division, Oak Ridge National Laboratory, Oak Ridge, Tennessee 37831, United States*

James R. Neilson − *Department of Chemistry, Colorado State University, Fort Collins, Colorado 80523, United States;* orcid.org/0000-0001-9282-5752

Ping Liu − *Department of Nanoengineering, University of California-San Diego, La Jolla, California 92093, United States;* orcid.org/0000-0002-1488-1668

Katsuyo Thornton − *Department of Materials Science and Engineering, University of Michigan, Ann Arbor, Michigan 48109, United States;* orcid.org/0000-0002-1227-5293

Complete contact information is available at: https://pubs.acs.org/10.1021/acs.chemmater.2c00303

Author Contributions

R.D.M. fabricated the bilayers, performed and analyzed the XRR, and analyzed the XPS data with guidance from G.M.V. R.C.D. and A.M. assisted in the setup and collection of XRR data, and A.M. and K.L.B. assisted in the analysis of the XRR data. V.P. performed and analyzed the AC impedance data with guidance from P.L. G.H. performed phase-field modeling calculations with guidance from D.M. and K.T. J.R.N. assisted in understanding the data and discussing reaction processes in metathesis reactions. R.D.M. wrote the manuscript with input from all the co-authors.

Notes

The authors declare no competing financial interest.

ACKNOWLEDGMENTS

This work was supported as part of GENESIS: A Next Generation Synthesis Center, an Energy Frontier Research Center funded by the U.S. Department of Energy, Office of Science, Basic Energy Sciences, under award number DE-

SC0019212. Research was performed at Oak Ridge National Laboratory (ORNL), managed by UT Battelle, LLC, for the U.S. Department of Energy (DOE) under contract DE-AC05-00OR22725. Use of the Stanford Synchrotron Radiation Lightsource, SLAC National Accelerator Laboratory, is supported by the U.S. Department of Energy, Office of Science, Office of Basic Energy Sciences, under contract no. DE-AC02-76SF00515. This work was performed in part at the San Diego Nanotechnology Infrastructure (SDNI) of UCSD, a member of the National Nanotechnology Coordinated Infrastructure (NNCI), which is supported by the National Science Foundation (grant ECCS-1542148). This manuscript has been authored by UT-Battelle, LLC, under contract no. DE-AC05-00OR22725 with the U.S. Department of Energy. The United States Government retains and the publisher, by accepting the article for publication, acknowledges that the United States Government retains a non-exclusive, paid-up, irrevocable, world-wide license to publish or reproduce the published form of this manuscript, or allow others to do so, for United States Government purposes. The Department of Energy will provide public access to these results of federally sponsored research in accordance with the DOE Public Access Plan (http://energy.gov/downloads/doe-public-access-plan).

REFERENCES

(1) Schleder, G. R.; Focassio, B.; Fazzio, A. Machine learning for materials discovery: Two-dimensional topological insulators. *Appl. Phys. Rev.* **2021**, *8*, 031409.
(2) Olsen, T.; Andersen, E.; Okugawa, T.; Torelli, D.; Deilmann, T.; Thygesen, K. S. Discovering two-dimensional topological insulators from high-throughput computations. *Phys. Rev. Mater.* **2019**, *3*, 024005.
(3) Xi, L.; Pan, S.; Li, X.; Xu, Y.; Ni, J.; Sun, X.; Yang, J.; Luo, J.; Xi, J.; Zhu, W.; Li, X.; Jiang, D.; Dronskowski, R.; Shi, X.; Snyder, G. J.; Zhang, W. Discovery of High-Performance Thermoelectric Chalcogenides through Reliable High-Throughput Material Screening. *J. Am. Chem. Soc.* **2018**, *140*, 10785−10793.
(4) Sheng, Y.; Deng, T.; Qiu, P.; Shi, X.; Xi, J.; Han, Y.; Yang, J. Accelerating the Discovery of Cu-Sn-S Thermoelectric Compounds via High-Throughput Synthesis, Characterization, and Machine Learning-Assisted Image Analysis. *Chem. Mater.* **2021**, *33*, 6918−6924.
(5) Stanev, V.; Oses, C.; Kusne, A. G.; Rodriguez, E.; Paglione, J.; Curtarolo, S.; Takeuchi, I. Machine learning modeling of superconducting critical temperature. *npj Comput. Mater.* **2018**, *4*, 29.
(6) Chamorro, J. R.; McQueen, T. M. Progress toward Solid State Synthesis by Design. *Acc. Chem. Res.* **2018**, *51*, 2918−2925.
(7) Stein, A.; Keller, S. W.; Mallouk, T. E. Turning down the heat: design and mechanism in solid-state synthesis. *Science* **1993**, *259*, 1558−1564.
(8) Narayan, A.; Bhutani, A.; Rubeck, S.; Eckstein, J. N.; Shoemaker, D. P.; Wagner, L. K. Computational and experimental investigation for new transition metal selenides and sulfides: The importance of experimental verification for stability. *Phys. Rev. B* **2016**, *94*, 045105.
(9) Todd, P. K.; McDermott, M. J.; Rom, C. L.; Corrao, A. A.; Denney, J. J.; Dwaraknath, S. S.; Khalifah, P. G.; Persson, K. A.; Neilson, J. R. Selectivity in Yttrium Manganese Oxide Synthesis via Local Chemical Potentials in Hyperdimensional Phase Space. *J. Am. Chem. Soc.* **2021**, *143*, 15185−15194.
(10) McDermott, M. J.; Dwaraknath, S. S.; Persson, K. A. A graph-based network for predicting chemical reaction pathways in solid-state materials synthesis. *Nat. Commun.* **2021**, *12*, 3097.
(11) Bianchini, M.; Wang, J.; Clément, R. J.; Ouyang, B.; Xiao, P.; Kitchaev, D.; Shi, T.; Zhang, Y.; Wang, Y.; Kim, H.; Zhang, M.; Bai, J.; Wang, F.; Sun, W.; Ceder, G. The interplay between thermodynamics and kinetics in the solid-state synthesis of layered oxides. *Nat. Mater.* **2020**, *19*, 1088−1095.
(12) Aykol, M.; Montoya, J. H.; Hummelshøj, J. Rational Solid-State Synthesis Routes for Inorganic Materials. *J. Am. Chem. Soc.* **2021**, *143*, 9244−9259.
(13) Miura, A.; Bartel, C. J.; Goto, Y.; Mizuguchi, Y.; Moriyoshi, C.; Kuroiwa, Y.; Wang, Y.; Yaguchi, T.; Shirai, M.; Nagao, M.; Rosero-Navarro, N. C.; Tadanaga, K.; Ceder, G.; Sun, W. Observing and Modeling the Sequential Pairwise Reactions that Drive Solid-State Ceramic Synthesis. *Adv. Mater.* **2021**, *33*, No. e2100312.
(14) Bonneau, P. R.; Jarvis, R. F.; Kaner, R. B. Rapid solid-state synthesis of materials from molybdenum disulphide to refractories. *Nature* **1991**, *349*, 510−512.
(15) Bonneau, P. R.; Jarvis, R. F.; Kaner, R. B. Solid-State Metathesis as a Quick Route to Transition-Metal Mixed Dichalcogenides. *Inorg. Chem.* **1992**, *31*, 2127−2132.
(16) Martinolich, A. J.; Neilson, J. R. Pyrite formation via kinetic intermediates through low-temperature solid-state metathesis. *J. Am. Chem. Soc.* **2014**, *136*, 15654−15659.
(17) Treece, R. E.; Gillan, E. G.; Kaner, R. B. Materials Synthesis Via Solid-State Metathesis Reactions. *Comments Inorg. Chem.* **1995**, *16*, 313−337.
(18) Todd, P. K.; Wustrow, A.; McAuliffe, R. D.; McDermott, M. J.; Tran, G. T.; McBride, B. C.; Boeding, E. D.; O'Nolan, D.; Liu, C.-H.; Dwaraknath, S. S.; Chapman, K. W.; Billinge, S. J. L.; Persson, K. A.; Huq, A.; Veith, G. M.; Neilson, J. R. Defect-Accommodating Intermediates Yield Selective Low-Temperature Synthesis of $YMnO_3$ Polymorphs. *Inorg. Chem.* **2020**, *59*, 13639−13650.
(19) Todd, P. K.; Neilson, J. R. Selective Formation of Yttrium Manganese Oxides through Kinetically Competent Assisted Metathesis Reactions. *J. Am. Chem. Soc.* **2019**, *141*, 1191−1195.
(20) Martinolich, A. J.; Kurzman, J. A.; Neilson, J. R. Circumventing Diffusion in Kinetically Controlled Solid-State Metathesis Reactions. *J. Am. Chem. Soc.* **2016**, *138*, 11031−11037.
(21) Bauers, S. R.; Wood, S. R.; Jensen, K. M. Ø.; Blichfeld, A. B.; Iversen, B. B.; Billinge, S. J. L.; Johnson, D. C. Structural Evolution of Iron Antimonides from Amorphous Precursors to Crystalline Products Studied by Total Scattering Techniques. *J. Am. Chem. Soc.* **2015**, *137*, 9652−9658.
(22) Bardgett, D.; Gannon, R. N.; Hamann, D. M.; Roberts, D. M.; Bauers, S. R.; Lu, P.; Johnson, D. C. Understanding the Reactions Between Fe and Se Binary Diffusion Couples. *Chem. Mater.* **2021**, *33*, 2585−2592.
(23) Cordova, D. L. M.; Johnson, D. C. Synthesis of Metastable Inorganic Solids with Extended Structures. *ChemPhysChem* **2020**, *21*, 1345−1368.
(24) Liu, J. P.; Kirchhoff, J.; Zhou, L.; Zhao, M.; Grapes, M. D.; Dale, D. S.; Tate, M. D.; Philipp, H. T.; Gruner, S. M.; Weihs, T. P.; Hufnagel, T. C. X-ray reflectivity measurement of interdiffusion in metallic multilayers during rapid heating. *J. Synchrotron Radiat.* **2017**, *24*, 796−801.
(25) Stevens, B. L.; Cohen, D. J.; Barnett, S. A. Structure and interdiffusion of epitaxial ZnO/ZnMgO nanolayered thin films. *J. Vac. Sci. Technol., A* **2008**, *26*, 1538−1541.
(26) Kontturi, E.; Lankinen, A. Following the kinetics of a chemical reaction in ultrathin supported polymer films by reliable mass density determination with X-ray reflectivity. *J. Am. Chem. Soc.* **2010**, *132*, 3678−3679.
(27) Zotov, N.; Feydt, J.; Savan, A.; Ludwig, A.; von Borany, J. Interdiffusion in Fe/Pt Multilayers: In Situ High Temperature Synchrotron Radiation Reflectivity Study. *Adv. Eng. Mater.* **2011**, *13*, 475−479.
(28) Aurongzeb, D.; Holtz, M.; Daugherty, M.; Berg, J. M.; Chandolu, A.; Yun, J.; Temkin, H. Influence of nanocrystal growth kinetics on interface roughness in nickel-aluminum multilayers. *Appl. Phys. Lett.* **2003**, *83*, 5437−5439.
(29) Singh, S.; Basu, S.; Bhatt, P.; Poswal, A. K. Kinetics of alloy formation at the interfaces in a Ni-Ti multilayer: X-ray and neutron

reflectometry study. *Phys. Rev. B: Condens. Matter Mater. Phys.* **2009**, *79*, 195435.
(30) Johnson, D. C. Controlled synthesis of new compounds using modulated elemental reactants. *Curr. Opin. Solid State Mater. Sci.* **1998**, *3*, 159−167.
(31) Anderson, M. D.; Thompson, J. O.; Johnson, D. C. Avoiding Binary Compounds as Reaction Intermediates in Solid State Reactions. *Chem. Mater.* **2013**, *25*, 3996−4002.
(32) Cotts, E. J.; Meng, W. J.; Johnson, W. L. Calorimetric study of amorphization in planar, binary, multilayer, thin-film diffusion couples of Ni and Zr. *Phys. Rev. Lett.* **1986**, *57*, 2295−2298.
(33) Miller, A. M.; Hamann, D. M.; Hadland, E. C.; Johnson, D. C. Investigating the Formation of $MoSe_2$ and $TiSe_2$ Films from Artificially Layered Precursors. *Inorg. Chem.* **2020**, *59*, 12536−12544.
(34) Regus, M.; Kuhn, G.; Polesya, S.; Mankovsky, S.; Alemayehu, M.; Stolt, M.; Johnson, D. C.; Ebert, H.; Bensch, W. Experimental and theoretical investigation of the new, metastable compound Cr_3Sb. *Z. Kristallogr.-Cryst. Mater.* **2014**, *229*, 505−515.
(35) Regus, M.; Mankovsky, S.; Polesya, S.; Kuhn, G.; Ditto, J.; Schürmann, U.; Jacquot, A.; Bartholomé, K.; Näther, C.; Winkler, M.; König, J. D.; Böttner, H.; Kienle, L.; Johnson, D. C.; Ebert, H.; Bensch, W. Characterization of Cr-rich Cr-Sb multilayer films: Syntheses of a new metastable phase using modulated elemental reactants. *J. Solid State Chem.* **2015**, *230*, 254−265.
(36) Rodewald, J.; Thien, J.; Pohlmann, T.; Hoppe, M.; Timmer, F.; Bertram, F.; Kuepper, K.; Wollschläger, J. Formation of ultrathin cobalt ferrite films by interdiffusion of Fe_3O_4/CoO bilayers. *Phys. Rev. B* **2019**, *100*, 155418.
(37) Zolotaryov, A.; Goetze, S.; Zierold, R.; Novikov, D.; Birajdar, B.; Hesse, D.; Nielsch, K. Temperature-Dependent Solid-State Reactions With and Without Kirkendall Effect in Al_2O_3/ZnO, Fe_2O_3/ZnO, and Co_XO_Y/ZnO Oxide Thin Film Systems. *Adv. Eng. Mater.* **2010**, *12*, 509−516.
(38) Choffel, M. A.; Kam, T. M.; Johnson, D. C. Substituent Effects in the Synthesis of Heterostructures. *Inorg. Chem.* **2021**, *60*, 9598−9606.
(39) Gunning, N. S.; Feser, J.; Beekman, M.; Cahill, D. G.; Johnson, D. C. Synthesis and Thermal Properties of Solid-State Structural Isomers: Ordered Intergrowths of SnSe and $MoSe_2$. *J. Am. Chem. Soc.* **2015**, *137*, 8803−8809.
(40) Li, D.; Schleife, A.; Cahill, D. G.; Mitchson, G.; Johnson, D. C. Ultralow shear modulus of incommensurate $[SnSe]_n[MoSe2]_n$ layers synthesized by the method of modulated elemental reactants. *Phys. Rev. Mater.* **2019**, *3*, 043607.
(41) Lin, Q.; Heideman, C. L.; Nguyen, N.; Zschack, P.; Chiritescu, C.; Cahill, D. G.; Johnson, D. C. Designed Synthesis of Families of Misfit-Layered Compounds. *Eur. J. Inorg. Chem.* **2008**, *2008*, 2382−2385.
(42) McAuliffe, R. D.; Yang, G.; Nanda, J.; Veith, G. M. Synthesis of metal chloride films: Influence of growth conditions on crystallinity. *Thin Solid Films* **2019**, *689*, 137520.
(43) McAuliffe, R. D.; Petrova, V.; McDermott, M. J.; Tyler, J. L.; Self, E. C.; Persson, K. A.; Liu, P.; Veith, G. M. Synthesis of model sodium sulfide films. *J. Vac. Sci. Technol., A* **2021**, *39*, 053404.
(44) Björck, M.; Andersson, G. GenX: an extensible X-ray reflectivity refinement program utilizing differential evolution. *J. Appl. Crystallogr.* **2007**, *40*, 1174−1178.
(45) Cahn, J. W. On Spinodal Decomposition. *Acta Metall.* **1961**, *9*, 795−801.
(46) Grosvenor, A. P.; Kobe, B. A.; Biesinger, M. C.; McIntyre, N. S. Investigation of multiplet splitting of Fe 2p XPS spectra and bonding in iron compounds. *Surf. Interface Anal.* **2004**, *36*, 1564−1574.
(47) Lennie, A. R.; Vaughan, D. J. Spectroscopic studies of iron sulfide formation and phase relations at low temperatures. *Mineral Spectroscopy*; The Geochemical Society, 1996; Vol. *5*, pp 117−131.
(48) Moulder, J. F.; Stickle, W. F.; Sobol, P. E.; Bobmben, K. D. *Handbook of X-ray Photoelectron Spectroscopy*; Perkin-Elmer Corporation: Eden Prairie, Minnesota, 1992.
(49) Savintsev, A. P.; Gavasheli, Y. O.; Kalazhokov, Z. K.; Kalazhokov, K. K. X-ray photoelectron spectroscopy studies of the sodium chloride surface after laser exposure. *J. Phys.: Conf. Ser.* **2016**, *774*, 012118.
(50) Fantauzzi, M.; Elsener, B.; Atzei, D.; Rigoldi, A.; Rossi, A. Exploiting XPS for the identification of sulfides and polysulfides. *RSC Adv.* **2015**, *5*, 75953−75963.
(51) Mapother, D.; Crooks, H. N.; Maurer, R. Self-Diffusion of Sodium in Sodium Chloride and Sodium Bromide. *J. Chem. Phys.* **1950**, *18*, 1231−1236.
(52) Harrison, L. G.; Morrison, J. A.; Rudham, R. Chloride ion diffusion in sodium chloride. Interactions between point imperfections at low temperatures. *Trans. Faraday Soc.* **1958**, *54*, 106−115.
(53) Laurance, N. Self-Diffusion of the Chloride Ion in Sodium Chloride. *Phys. Rev.* **1960**, *120*, 57−62.
(54) Zhang, B.; Li, C.; Shan, S. Thermodynamic calculation of self-diffusion in sodium chloride. *Phys. Chem. Miner.* **2016**, *43*, 371−376.

https://doi.org/10.1021/acs.chemmater.2c00303
Chem. Mater. 2022, 34, 6279−6287